The Cryosphere Discuss., https://doi.org/10.5194/tc-2018-262
Manuscript under review for journal The Cryosphere
Discussion started: 25 January 2019

The Cryosphere Discussions
Open Access

Estimation of turbulent heat flux over leads using satellite thermal images

Meng Qu[1], Xiaoping Pang[1], Xi Zhao[1,2], Jinlun Zhang[2], Qing Ji[1], Pei Fan[1]

[1]Chinese Antarctic Center of Surveying and Mapping, Wuhan University, Wuhan 430079, China
[2]Applied Physics Laboratory, Polar Science Center, University of Washington, Seattle, Washington 98195-3770, USA

Correspondence to: Xi Zhao (xi.zhao@whu.edu.cn)

Abstract. Sea ice leads are an important feature in pack ice in the Arctic. Even covered by thin ice, leads can still serve as the prime window for heat exchange between the atmosphere and the ocean, especially in winter seasons. Lead geometry and distribution in the Arctic have been studied in previous studies using optical or microwave remote sensing data. But turbulent heat flux over lead area has only been measured on site during a few special expeditions. In this study, we derive turbulent heat flux through leads at different scale using a combination of surface temperature and lead distribution from remote sensing images and meteorological parameters from a reanalysis dataset. Firstly, ice surface temperature was calculated from Landsat-8 Thermal Infrared Sensor (TIRS) and MODIS thermal images using split-window algorithm at 30 m and 1 km scales, respectively, then lead pixels are segmented from colder ice. Heat flux over lead area was estimated using two empirical models, including bulk aerodynamic formulae and a fetch-limited model with lead width from Landsat-8. Results show that, even though lead area from MODIS is a little larger, the length of leads is underestimated by 72.9% in MODIS data compared to that from TIRS due to the inability to resolve small leads. Heat flux estimated from Landsat-8 TIRS data using bulk formulae is 42.33% larger than that from MODIS data. When fetch-limited model was applied, turbulent heat flux calculated from TIRS data is 31.87% higher than that from bulk formulae. In both cases, small leads account for more than a quarter of total heat flux over lead, mainly due to its large area, though the heat flux estimated using fetch-limited model is 42.26% larger. More contribution from small leads can be expected at larger air-ocean temperature difference and stronger winds.

1 Introduction

Leads are linear structures of ocean surface within pack ice that is exposed to atmosphere during an opening event caused by various forces, such as wind and water stresses. In winter, thin ice forms quickly in newly opened leads due to the large temperature difference between the ocean and the atmosphere (Kwok, 2001). The opening of leads breaks the continuity of insulating ice and creates windows for a stronger air-ocean interaction. Newly opened leads are the main source of ice production, brine rejection, and heat transfer from the ocean to the atmosphere (Alam and Curry, 1998). The rate of turbulent heat transferred over open water could be two orders of magnitude larger than that through mature ice (Maykut, 1978). Although decreasing rapidly with growing ice thickness, ice growth rates can still be an order of magnitude larger for 50-cm-thick young ice than for 3-m-thick ice (Maykut, 1986). In the central Arctic, open water usually comprises no more than 1% of the ice pack area during the winter seasons. However, open water, together with thin ice (< 1 m) that is estimated to be 10% of the whole ice area, contributes to more than 70% of the upward heat flux (Maykut, 1978; Marcq and Weiss, 2012).

Leads also allow more surface absorption of radiation in late spring and summer due to their lower albedo compared to thick ice. This will accelerate sea ice thinning in summer and delay refreezing in early winter, therefore decreasing the mechanical strength of the ice cover and allowing even more fracturing, larger drifting speed and deformation, and a faster export of sea ice to lower latitudes (Rampal et al., 2009). As the ice pack is getting thinner (Kwok and Rothrock, 2009) and more mobile (Spreen et al., 2011), favorable for deformation and opening, more intensive network and stronger influence of leads are expected.

Regarding the detection of leads in satellite imagery, Lindsay and Rothrock (1995) promoted the concept of potential open water, which requires both temperature and albedo difference between ice surface pixel and open water tie-point. Röhrs and Kaleschke (2012) developed a retrieval algorithm to obtain Arctic lead concentration, similar to sea ice concentration, based on different emissivities of thin ice at two microwave frequencies available for AMSR-E. The algorithm could provide sub-pixel information of lead distribution. But the resolution is still too coarse to detect small leads prevailing in pack ice. Willmes and Heinamann (2015) mapped pan-Arctic lead distribution at 1km resolution using of a single parameter, local temperature anomaly $\triangle T_S$, to identify leads from surrounding thick ice. Other remote sensing data, including altimetry, high resolution optical and SAR images were also used to identify leads in limited areas due to constraints of cloud contamination and data acquisition restriction (Key et all., 1993; Miles and Barry, 1998; Kwok, 2001; Weiss and Marsan, 2004; Wernecke and Kaleschke, 2015; Murashkin et al., 2018).

Regardless of spectral characteristics used for detection of leads, scale dependence of lead statistics was explored in a few studies (Key et al., 1994; Weiss and Marsan, 2004; Marson et al., 2004). Key et al. (1994) studied the effects of sensor's field-of-view (FOV) using degraded optical images from Landsat Multi-Spectral Scanner (MSS). They suggested that the mean lead width expands and the lead fraction drops as the pixel size builds up in gradually degraded images. Assuming that narrow leads had a larger heat flux transfer rate than wider leads, estimated turbulent heat flux was reduced by 45% as the FOV was degraded from 80 m to 640 m, mainly due to reduced lead fraction.

More often than not, bulk aerodynamic formulae are used in climate models to generalize the turbulent heat flux from open water in Arctic pack ice (Lindsay and Rothrock, 1994; Walter et al. 1995). The bulk formulae attribute heat flux from leads to wind speed at certain height, the temperature difference between the surface and the atmosphere, and a turbulent transfer coefficient for heat, which is a function of the stability of the near-surface atmosphere and the roughness of the surface. Sensible heat flux was estimated in this approach by Lindsay and Rothrock (1994) using surface temperature retrieved from Advanced Very High Resolution Radiometer (AVHRR). While observations suggest that, for small leads down to dozens of meters in width, the discontinuity between leads and pack ice causes the creation of a thermal internal boundary layer (TIBL) in the bottom atmosphere and the thickness of this TIBL depends mainly on lead width or fetch (Venkatram, 1977; Andreas et al., 1979). Fetch limited models (Alam and Curry; 1997; Andreas and Cash,1999) for turbulent heat flux over small leads were developed based on a few observations. Besides, a power law distribution of lead width was also reported in various studies (Wadhams, 1981; Wadhams et al., 1985; Lindsay and Rothrock, 1995), indicating that small leads are prevailing in the Arctic. Impacts of lead width on heat flux were reported by Maslanik and Key (1995) and Marcq and Weiss (2012) using a different width distribution model. However, fetch-limited models have not been applied to surface temperature fields retrieved from remote sensing imagery to estimate turbulent heat flux at regional scale due to the coarse resolution of operational thermal sensors. Fortunately, the launch of Landsat-8 in February 11th, 2013 has provided a unique opportunity for estimation of turbulent heat flux with finer-resolution temperature fields.

In this paper, we will retrieve lead distribution using thermal images from two sensors (MODIS and TIRS aboard Terra and Landsat-8, respectively) at different resolution scales. Then we will estimate heat flux over leads with remote sensing temperature field using both the bulk formulae and a fetch-limited model proposed by Andras and Cash (1999). With the result, we will analyze how the scale property of leads may impact the calculation of heat exchange through leads.

2 Data

Three successive scenes of Level 1 terrain-corrected (L1T) Landsat-8 TIRS images and one corresponding MODIS images were used in this study (Table 1). As shown in Fig. 1, the mosaic image of the three TIRS scenes covers an area of about 98000 km^2 in the east Beaufort Sea, with floes and leads of various lengths and widths spread in the region.

The Landsat 8 satellite is in the same near-polar, sun-synchronous,705 km circular orbit and position as the Landsat 5 satellite decommissioned in 2013. Landsat 8 data are acquired in 185 km swaths and segmented into 185 km × 180 km scenes defined in the second World-wide Reference System (WRS-2) of path (ground track parallel) and row (latitude parallel) coordinates also used by the Landsat 4, 5 and 7 satellites (Arvidson et al., 2001). TIRS instrument is one of the major payloads aboard the Landsat 8 satellite which can observe the ocean surface at a resolution of 100 m by using the split-window thermal infrared bands, comparable to MODIS thermal infrared bands at a resolution of 1000 m. The two narrower thermal infrared channels in the atmospheric window enable the application of the widely used split-window algorithm (SWA) in ice surface temperature (IST) retrieval rather than the single-channel method used for TIRS predecessors.

Note that the TIRS bands at 100m resolution are resampled by cubic convolution to 30 m and co-registered with the Operational Land Imager (OLI) spectral bands in L1T product. Apart from the TIRS thermal bands, top of atmosphere reflectance from Landsat-8 near-infrared band, was used for classification between ice and open water in surface temperature retrieval. Panchromatic band with a resolution of 15m, was used as validation data for lead detection in this study.

Corresponding 10m wind vector, 2m air temperature and dewpoint temperature from ECMWF ERA-interim reanalysis data set are also used. The ERA-interim reanalysis dataset has a fine spatial resolution of 0.125° (~10km in study area) and a temporal resolution of 3 hours. The time difference between reanalysis data and Landsat-8 or MODIS images is within half an hour. 10m wind vectors from ERA-interim are transferred to wind magnitude at reference height of 2 m in accordance with air temperature data.

3 Method

3.1 IST Retrieval

An SWA for IST retrieval was first developed for AVHRR (Key et al. 1997) and adopted for MODIS thermal images with a different set of coefficients (Hall et al. 2001). The equation is as followed:

$$\mathrm{IST} = \mathrm{a} + \mathrm{b}T_{31} + c(T_{31} - T_{32}) + d[(T_{31} - T_{32})(\sec q - 1)] \tag{1}$$

where T_{31} and T_{32} are brightness temperature from MODIS thermal bands B31 and B32; a, b, c and d are coefficients developed for specific sensors using radiance transfer model; q represents the incidence angle, and sec q is the secant of q.

Since there is no special SWA available for sea ice surface temperature retrieval from Landsat-8, a land surface temperature formulation (Du et al. 2015) developed for a wide range of surface type, including ice and snow, was used:

$$T_s = b_0 + \left(b_1 + b_2\frac{1-\varepsilon}{\varepsilon} + b_3\frac{\Delta\varepsilon}{\varepsilon^2}\right)\frac{T_i+T_j}{2} + \left(b_4 + b_5\frac{1-\varepsilon}{\varepsilon} + b_6\frac{\Delta\varepsilon}{\varepsilon^2}\right)\frac{T_i-T_j}{2} + b_7(T_i - T_j)^2 \tag{2}$$

where T_i and T_j are the brightness temperatures measured in channels i (~11.0 μm) and j (~12.0 μm), respectively; ε is the mean emissivity of the two channels (i.e., $\varepsilon = 0.5\,[\varepsilon_i + \varepsilon_j]$), while $\Delta\varepsilon$ is the emissivity difference between the channels (i.e., $\Delta\varepsilon = \varepsilon_i - \varepsilon_j$); b_k (k = 0, 1, ... 7) are the algorithm coefficients derived from simulated dataset.

As reported in previous studies (Montanaro et al., 2014a; Barsi et al., 2014; Montanaro et al., 2014b; Montanaro et al., 2014c), thermal infrared radiance measured by Landsat-8 TIRS suffers from straylight, which is caused by out-of-field radiance that scatters onto the detectors thereby adding a non-uniform/banding signal across the field-of-view. The magnitude of this extra signal can be ~8% or higher (band 11) and is generally twice as large in band 11 as it is in band 10. Though correction algorithms for this artifact have been developed and applied in the new version of level L1T Landsat-8 data (Montanaro et al., 2015), and the straylight artifact in current product is reduced by half on average (Gerace and Montanaro, 2017). However, straylight artifact could be amplified in surface temperature map when SWA was used, temperature error could be 0~2K or more even after the correction algorithm was applied (Gerace and Montanaro, 2017), this will certainly impact lead detection from IST maps.

A post-processing procedure utilizing the linear pattern of straylight artifact is applied to remove this banding noise. Firstly, a median temperature is determined for each image pixel from a long enough along-track-only neighborhood. Then a noise image could be obtained by detrending this median image (Eppler and Full, 1992), thus the surface temperature image from SWA could be improved for lead detection.

3.2 Lead detection

In remote sensing images, leads (thin ice and open water) are represented by negative albedo in optical range, negative brightness temperature anomaly in near infrared (NIR) and a positive surface temperature anomaly compared to the surrounding thick ice (Fett et al., 1997). Variance caused by uneven illumination, view angle and air temperature should also be taken into account.

Willmes and Heinemann (2015) reported the use of surface temperature anomaly to detect leads. The temperature anomaly $\triangle T_S$ for each IST pixel is defined as deviation from the median in a square neighborhood, thus temperature variation due to air temperature field can be removed. This can be expressed in following equation:

$$\Delta T_0 = IST - Median_w \qquad (3)$$

where $Median_w$ represents the median IST in a square neighborhood with side length of w. This equation was adopted to Landsat-8 IST map using median from an along-tract-only linear neighborhood to further minimize the straylight artifact. Since the median temperature is selected as background temperature, the length w should be at least twice as large as the largest lead width within the image area (or along track) to reserve lead profile and reduce temperature gradient caused by varying air condition across the image.

Generally, surface temperature anomaly for thick ice follows a normal distribution with a mean of zero, thus any large deviation from the mean can be assumed as a potential lead and extracted using a proper threshold. Several image-based threshold selection techniques for a binary lead segmentation were compared in Willmes and Heinemann (2015), and an iterative threshold selection method (Ridler and Calvard, 1978) was recommended for extracting leads from temperature anomaly map. However, any image-based threshold method provides a threshold that may vary significantly due to temperature noise and lead distribution. For consistency in different scales, several threshold methods were compared for lead detection in both MODIS and TIRS temperature maps.

Lead widths were calculated for every lead pixel using an orthogonal system (vertical: south-north and horizontal: west-east, Fig. 2), and a minimum extent in two orthogonal directions was selected for the pixel, i.e., $x'=\min(x_1, x_2)$. Since the orientation of single lead is unknown, this method tends to overestimate lead width due to the mismatch of preset direction and the orientation of lead (Key and Peckham, 1991), but the usage of orthogonal system will contain the error ($x' \leq \sqrt{2}x$) and thus suffice the limited used of lead width in our study.

3.3 Heat flux model used for lead area

Turbulent heat flux between the Arctic ocean and the atmosphere, including sensible (F_s) and latent (F_l) heat fluxes, is mostly dominated by heat flux over open water and thin ice, which constitute leads in pack ice and polynya in coastal area. Turbulent heat flux over leads can be estimated using bulk aerodynamic formulae or fetch-limited model developed based on field observations.

3.3.1 Bulk aerodynamic formulae

Assuming that temperatures in the atmospheric boundary layer are determined by the heat balance over the thicker ice and the rate of turbulent heat change does not vary significantly across the narrow areas of leads, then the turbulent heat fluxes are mainly determined by temperature and humidity differences between the surface and atmosphere at reference height r (Maykut, 1978). The sensible heat flux (F_s) and latent heat flux (F_l) are given by the following bulk formulae:

$$F_s=\rho_a c_p C_s u(T_a-T_0) \qquad （4）$$

and

$$F_l=\rho_a L_v C_e u(Q_a-Q_0) \qquad （5）$$

where ρ_a is the air density; c_p is the specific heat at constant pressure; C_s is the sensible heat transfer coefficient; C_e is the evaporation coefficient; L_v is the latent heat of vaporization, u, T_a and Q_a are wind speed, air temperature and specific humidity at reference height r. T_0 and Q_0 are air temperature and specific humidity at the surface. Assuming that air at the surface of ice or water is always saturated, the specific humidity at surface can be derived as:

$$Q_0 = \frac{0.622 e_{s0}}{p-0.378 e_{s0}} \qquad (6)$$

where p is the air pressure, e_{s0} represents the saturated vapor pressure at surface temperature T_0:

$$e_{s0} = e_0 10^{\frac{at}{b+t}} \qquad (7)$$

where e_0 represent saturate vapor pressure at 0°C, approximately 611hPa, t is temperature in Celsius, a and b are coefficient (for water surface, a = 7.5, b=237.3 K; for ice, a=9.5, b=265.5 K). These equations are also applied for specific humidity at reference height *r* = 2 m using dewpoint temperature data from ERA-interim. Note that the heat flux in formulae (4) and (5) are directed from atmosphere to ocean.

3.3.2 Fetch-limited model

When air travels from a cooler surface to a warmer one, a convective atmospheric TIBL forms and thickens with distance downwind of the surface discontinuity or fetch *X* (Stull, 1988; see Fig. 2). As the wind blows over water (or thin ice), the near -surface air gets warmer with more vapor, while new ice accumulates at downwind side of the lead, progressively narrows and seals the window. Thus, the temperature and humidity differences between the air and the surface decreases. Since the sensible and latent heat fluxes are proportional to the temperature and humidity difference, respectively, turbulent heat transfer also recedes with increasing lead width or fetch. This means, with the same surface condition, larger lead is less efficient in heat exchanging in unit area, as shown in Fig. 3.

The dependence of H_s and H_l on fetch *X* was estimated in several studies (Andreas and Murphy, 1986; Alam and Curry, 1997; Andreas and Cash, 1999). Andreas and Cash (1999) give direct formulations of the heat fluxes as a function of the lead width *X* based on data fitting from three sets of measurements. For free convection conditions in large fetch:

$$\mathrm{F}_{s(\mathrm{X})}=\mathrm{C}_{*}\rho_{\mathrm{a}}\mathrm{C}_{\mathrm{p}}\mathrm{D}(\mathrm{T}_{\mathrm{s}}-\mathrm{T}_{a})/\Delta \mathrm{z}_{\mathrm{T}} \tag{8}$$

$$\mathrm{F}_{L(\mathrm{X})}=\mathrm{C}_{*}\rho_{\mathrm{a}}\mathrm{L}_{v}\mathrm{D}_{\mathrm{w}}(\mathrm{Q}_{\mathrm{s}}-\mathrm{Q}_{\mathrm{a}})/\Delta \mathrm{z}_{\mathrm{Q}} \tag{9}$$

where *D* and D_w are the molecular diffusivities of heat and water vapor in air, respectively; $\Delta \mathrm{z}_{\mathrm{T}}$ and $\Delta \mathrm{z}_{\mathrm{Q}}$ are length scales for heat and humidity, respectively, which consider the viscosity of air and the buoyancy difference between the surface and the reference height *r*:

$$\Delta \mathrm{z}_{\mathrm{T}}=\left(\frac{v\mathrm{D}}{\Delta \mathrm{B}}\right)^{1/3} \tag{10}$$

$$\Delta \mathrm{z}_{\mathrm{Q}}=\left(\frac{v\mathrm{D}_{\mathrm{w}}}{\Delta \mathrm{B}}\right)^{1/3} \tag{11}$$

$$\Delta \mathrm{B}=\frac{\mathrm{g}}{\overline{\mathrm{T}}}\left(\Delta \mathrm{T}+\frac{0.61\overline{\mathrm{T}}\Delta \mathrm{Q}}{1+0.61\overline{\mathrm{Q}}}\right) \tag{12}$$

where $\Delta \mathrm{B}$ is the buoyancy difference, $\Delta \mathrm{T}$ and $\Delta \mathrm{Q}$ are the difference of temperature and specific humidity between surface and air at reference height r, respectively, $\overline{\mathrm{T}}$ and $\overline{\mathrm{Q}}$ are the average temperature and specific humidity between them.

The coefficient C_* is a function of stability, which facilitates the generalization of the flux formulae (8), (9) to the transition between free and forced convection, thus applicable to smaller fetch. C_* is estimated using lead and polynya data and used to calculate both sensible and latent heat fluxes:

$$C_{*}=\frac{0.3}{0.4-h/L}+0.15 \tag{13}$$

$$h=0.82\ln X+0.02 \tag{14}$$

$$L^{-1}=8.0*\left(\frac{0.65}{r}+0.079-0.0043r\right)*Ri_b \tag{15}$$

$$Ri_b=-\frac{rg}{\overline{T}}\frac{T_s-T_r}{u_r^2} \tag{16}$$

where *h* is the depth of TIBL in meters as a function of lead width *X*, and *L* is the Obukhov length. *L* is a length scale of stability, it’s negative for unstable stratification, while its magnitude rises with instability. Ri_b and u_r represent Richardson number and wind speed at reference height *r*, and *g* is the gravitational constant.

In spite of the width of a lead, the model suggests that heat flux from a lead is also sensitive to meteorological parameters. As shown in Fig. 3, simulation shows that for the narrowest lead from TIRS (*X*=30m), turbulent heat flux, especially sensible heat, rises quickly with larger △t and stronger wind.

Most importantly, assuming a constant temperature difference together with a steady crossing wind, heat flux decreases with increasing fetch, and becomes saturated for lead width great than 1km, as depicted in Fig. 4. Since the air temperature interpolated from the grid data of the ERA-Interim with 0.125° resolution, shows no signal of heating from TIBL caused by leads. The application of fetch-limited model is likely to improve the accuracy of estimated turbulent heat flux. As the fetch dependence of heat flux over lead is negligible for lead width greater than 1km, thus this model was applied to TIRS data only.

4 Result

4.1 Ice surface temperature

IST maps retrieved from TIRS and MODIS using eq. (1) and (2) are shown in Fig. 5. Temperature signature of small leads in the north part of the image area is largely reduced in MODIS IST map due to its coarse resolution and heterogeneous pixels, compared to that from TIRS. In the meantime, the banding effect of straylight is very obvious in TIRS IST map. This artifact was detected and removed by using a median from along-track linear neighborhood and detrend of the median image (Fig. 6). Corrected TIRS IST map is also shown in Fig. 5 for comparison.

Although the median and artifact images show a little bias around large leads, corrected TIRS IST map is very smooth compared to uncorrected one and more suitable for lead detection using a threshold and heat flux calculation. Scatter plots of IST from MODIS and TIRS before and after correction are shown in Fig. 7. The correlation of IST from two sensors estimated by interpolation of MODIS IST to TIRS scale (30 m), is quite good with a Pearson coefficient above 0.890 (0.902 and 0.896 before and after correction for straylight). The primary coefficient of linear regression is improved from 1.025 to 1.004 before and after correction, indicating that the corrected TIRS IST is in better agreement with MODIS. However, the RMSE from regressions increased from 1.216 K to 1.233 K. It also reveals that, for the 250K~270K temperature range, IST retrieved from TIRS is generally 0.61~0.70K higher than that from MODIS.

4.2 Sea ice lead retrieval

Regional temperature anomaly maps calculated from IST maps are shown in Fig. 8. The mean surface temperature anomaly is 0.116 K with a standard deviation (Std) of 1.180 K for MODIS and 0.283 K with a Std of 1.619 K for TIRS.

Binary lead maps were generated using iterative thresholds (Fig. 9). Large floes and small leads dominate the northern part of the images where temperature is lower, while two very large leads can be observed in the southern portion. The maps illustrate that lead binary retrieved from MODIS captures major lead structure, but small leads are missed in most case compared to lead detected from TIRS.

Lead area estimated from MODIS is 8074.0 km^2 which account for 8.25% of the frame area (~98000 km^2), for TIRS, 7376.2 km^2 and 7.53%. Validation with Landsat-8 panchromatic images show that large leads tend to be amplified by blurred mixed pixels along boundaries, while small leads are neglected due to the coarse resolution of MODIS.

4.3 Lead width

In our study, lead width was calculated for every lead pixel in the binary maps from MODIS and TIRS and divided into three categories (Table 2), including small leads (width≤1km), medium leads (1km<width≤5km) and large leads(width>5km). The width distribution of leads from MODIS and small leads from TIRS are plotted in Fig. 10 using the length of leads. Similar to the concept of number density, the length of each lead width, could be fitted with a power law distribution with exponents of 2.241 for large leads from MODIS and 2.346 for leads from TIRS. The power law distribution indicates that narrow leads are prevalent, while larger exponent implies that smaller leads are more dominant at TIRS scale.

Total length of leads with various widths is 10150.3 km from TIRS, including 8502.2 km (83.76%) from small leads with width less than 1 km, comparing to total length of 2746.4 km from MODIS, where the narrow leads (1km wide) only account for 1050.0 km (38.23%). Total length of leads is underestimated by 72.9% in MODIS data compared to that from TIRS. As for the area of leads, small leads (width < 1km) account for 34.54% of total lead area from TIRS, while only 13.00% of lead area in MODIS comes from the narrow leads (Table 2).

4.4 Heat flux over leads

IST described in section 4.1 and lead width from TIRS (section 4.3) were used in bulk formulae and fetch-limited model along with ERA-interim reanalysis data to estimate turbulent heat flux through leads. For consistency, the estimated heat flux is positive from ocean to atmosphere.

4.3.1 Heat flux using bulk formulae

Turbulent heat flux over lead area is obtained by summing up sensible and latent heat flux from equations (4) and (5) using IST and lead maps retrieved from MODIS or TIRS (Fig. 11). Statistic in Table 2 reveals that total heat flux over lead calculated using TIRS IST and lead distribution, is 6.59×10^{11} W over the total area of 7376.2 km^2, 42.33% larger than that from MODIS data (4.63×10^{11} W). Small leads account for 1.68×10^{11} W (25.54%) of total heat flux in TIRS data, more than five times the heat flux from the narrow lead category in MODIS (3.28×10^{10}W, 7.08%).

4.3.2 Fetch-limited heat flux

Since the width-dependent heat flux model is valid for limited width range, this model was applied to Landsat-8 data only. As we can see in Fig. 11 and Table 3, total heat flux over leads estimated by fetch-limited model is 8.69×10^{11} W, 31.87% higher than that from bulk formulae i.e. 6.59×10^{11} W, among which 33.8% of the increase comes from the small lead class. In both cases, small leads account for a quarter or more of total heat flux over all leads in both models, due to its large area, though the heat flux estimated using fetch-limited model is 2.39×10^{11} W, 42.26% larger compared to 1.68×10^{11} W from bulk formulae. For comparison, the estimated heat fluxes from medium and large leads class also increase by 32.29% and 24.06%, respectively, when fetch-limited model was used. However, turbulent heat flux contribution from large lead is reduced from 34.67% to 32.62%, while contribution from small lead increases from 25.54% to 27.46%. Nonetheless, the fact that large leads with width greater than 5km, account for 27.16% of total lead area, but contribute more than 32% of total heat flux over lead, is somehow contradictive with the fetch-limited theory.

Inspection of input data revealed that, the 2m air temperature from ERA-interim has almost the same mean value around 262K as the surface temperature from Landsat-8. The temperature difference between air and the surface, i.e., △t, spreads from 1.58 to 12.38K, with a mean of 4.88K, along with a wind speed range from 3.8 to 7.7 m/s in the area. The distribution of air temperature and surface temperature of leads are plotted in Fig. 12. The temperature difference over narrow leads is too small to obtain a robust estimation of turbulent heat flux.

4.3.3 Conditional heat flux test

For comparison, a test using preset meteorological conditions was performed on the TIRS lead binary map. With a wind speed of 5 m/s at 2 m height and temperature difference of 5 K or 10 K, total heat fluxes from both models were calculated for leads with width range from 30m to 5km (Fig. 13), and summarized in Table 4. Note that lead width is in a logarithmic scale.

Clearly, overall turbulent heat flux estimated using fetch-limited model is always higher than that using bulk formulae with the same input. For both models, estimated turbulent heat fluxes with △t of 5K or 10K, peak at a smaller width (270m) than the 360m using △t obtained from TIRS IST and air temperature from ERA-interim. Compared to the real situation with △t range from 1.58 to 12.38K, although overall turbulent heat flux estimated at △t=5K is lower, more heat flux is effused from small leads with width less than 600m.

The distribution of turbulent heat fluxes estimated using bulk formulae with △t of 5K or 10K, depends on the areal fraction from each lead category. Contribution from leads with width greater than 1km converges to lower end with fluctuation. As expected, the estimated total heat flux of 1.00×10^{12} W at △t=10K is about twice as that at △t=5K (5.29×10^{11} W).

As for the fetch-limited model, small leads are found to have larger contribution at higher △t, i.e. 2.78×10^{11} W (36.54%) and 5.91×10^{11} W (37.18%) at △t of 5 K and 10 K, respectively, compared to its areal fraction of 34.54% in Table 4. More contribution from small leads can be expected at larger temperature difference and stronger wind in winter.

5 Discussion

5.1 Threshold method

Operational definition of lead is fracture or passageway through ice that is navigable by surface vessels (Canadian Ice Service, 2005; World Meteorological Organization, 2014). However, within any optical, thermal or microwave image, the radiometric signature of a narrow lead with open water may be identical to that of a wider lead with thin ice. In most studies involving the utility of remote sensing data, any linear features of open water or thin ice within pack ice are regard as leads for convenience (Fetterer and Holyer, 1989; Fily and Rothrock 1990; Lindsay and Rothrock, 1995). Due to the confusion of lead definition in remote sensing images and the need to extract lead from background, threshold segmentation was frequently used for lead detection from various satellite sensors and images (Eppler and Full, 1992; Lindsay and Rothrock, 1995; Weiss and Marsan, 2004; Marcq and Weiss, 2012). Several threshold selection techniques for a binary lead segmentation were presented in a previous study (Willmes and Heinemann, 2015), however, threshold given by image-based method may vary significantly depending on noise level (caused by air temperature variance) and lead distribution.

In our study, a set of thresholds was tested for extracting leads from temperature anomaly maps from MODIS and Landsat-8, areal fractions of leads from fixed thresholds, Std thresholds, and an iterative threshold are shown in Table 5. Since the anomaly maps from two sensors have different means and standard deviations, mainly due to different definition of neighborhood in calculation of △t, the result from a fixed threshold might be biased. Iterative thresholds from both anomaly maps are a little larger than their first std. Any larger threshold tends to underestimate lead distribution. While lower threshold allows more pixel detected as leads, false leads caused by air temperature variance tend to occur. Validation with Landsat-8 Panchromatic images shows that iterative threshold detects most lead structure (89.5%) and exhibits better resistance against air temperature noise. Thus, the iterative thresholds are selected for lead extraction in this study.

5.2 Width distribution of leads

Lead geometry and distribution in the Arctic have been studied using optical and microwave remote sensing data (Fily and Rothrock, 1990; Lindsay and Rothrock, 1995; Tschudi et al., 2002). A simple one-parameter exponential model was used for number density distribution of lead width (Key and Peckham, 1991; key et al., 1994; Maslanik and Key, 1995):

$$f_{(w)} = \frac{1}{\lambda} e^{\frac{-w}{\lambda}} \quad (17)$$

where *w* is width of lead, the single parameter λ is the mean lead width. But a mean lead width can be oversimplified in a diverse circumstance. Lindsay and Rothrock (1995) reported the power law distribution of lead width in AVHRR imagery:

$$N_{T(w)} = aw^{-b} \quad (18)$$

where $N_{T(w)}$ is the number density of leads of width w per kilometer of width increment. The exponent *b* indicates the relative frequency of large and small leads, while the coefficient *a* is directly related to the lead concentration and the range of widths over which the power law is thought to apply. The annual mean of exponent b was found to be 1.60 using AVHRR images (Lindsay and Rothrock,1995). Larger values of b were reported using data with better resolution: 2 and 2.29 for submarine sonar observation in Fram Strait (Wadhams, 1981) and Davis Strait (Wadhams et al, 1985) when 100m bin width was used, 2.1~ 2.6 for 20m SPOT image in orthographic direction using different threshold (Marcq and Weiss, 2012). Note that most of these studies using only width samples crossed by limited linear transect.

In our study, although lead width follows the same power low distribution at both scales, the fitted exponents vary from 0.882 to 2.094 at resolution from 30m to 1km. Since the 30m L1T images were resampled from original 100m TIRS data, actual distribution of leads with width less than 100m is debatable. In our calculation, lead width was assigned to every pixel across the lead instead of a fitted distribution model, and used in fetch-limit heat flux calculation. As a result, heat flux across a single lead may vary according to the surface temperature, as can be seen in the largest lead in Fig. 11.

5.3 Application of fetch-limited heat flux model

Our results suggest that, heat flux contribution from small leads mainly results from its large length, or number density, and vast area, instead of its efficiency. Though small leads are more efficient for heat exchanging between the ocean and the atmosphere, thin ice growing in newly opened leads may quickly cover the exposed ocean surface, thus reducing heat exchange. Moreover, due to the mixture of subpixel lead and thick ice, the surface temperature of some pixels in small leads is much lower than the freezing point.

Besides, wind direction should also be considered. In our study area, the main direction of wind from the reanalysis dataset is roughly perpendicular to the dominated orientation of leads. Therefore, wind magnitude instead of wind vector was used in our study.

Our result suggests that, with surface temperature field from remote sensing, fetch-limited model can be used for estimation of turbulent heat flux on regional scale. However, since the fetch-limited model proposed in Andreas and Cash (1999) was established based on mainly a few observations over open lead and polynya, while most lead pixels detected using temperature anomaly in our study is likely covered by thin ice (surface temperature <270K, Fig. 12). Near surface air temperature with finer resolution is needed for validation of the turbulent heat flux estimated using fetch-limited model before extensive application.

6 Conclusion

Although the same local temperature anomaly and threshold method were applied, leads retrieved at MODIS and Landsat-8 TIRS resolution scales present very different geometry and distribution. Over the studied area, general length of leads is 10150.3 km from TIRS, including 8502.2 km (83.76%) from small leads with width less than 1 km. This is in contrast to the total length of 2746.4 km from MODIS, where the narrow leads (1km wide) only account for 1050.0 km (38.23%). As for the area of leads, small leads (width < 1km) account for 34.54% of the total lead area from TIRS, while only take up 13.00% of the total lead area in MODIS. Although lead width follows the same power low distribution at both scales, the fitted exponents vary from 2.241 to 2.346.

When the same bulk aerodynamic formulae were applied with the reanalysis dataset, heat flux estimated using TIRS data is 6.59×10^{11} W, 42.33% larger than that from MODIS data (4.63×10^{11} W). Small leads account for 1.68×10^{11} W (25.54%) of total heat flux over all leads in TIRS data, more than five times the heat flux from the narrow lead category in MODIS (3.28×10^{10}W, 7.08%).

Turbulent heat flux over leads estimated by fetch-limited model is 8.69×10^{11} W, 31.87% higher than that from bulk formulae (6.59×10^{11} W). In both cases, small leads account for about a quarter of total heat flux in both models, due to its large area, though the heat flux estimated using fetch-limited model is 42.26% larger. More contribution from small leads can be expected at larger temperature difference and stronger wind conditions. Near surface air temperature with finer resolution is still needed for validation of turbulent heat flux estimated using fetch-limited model before extensive application.

Appendix A

Validation using Landsat-8 Panchromatic image:

Top of atmosphere (TOA) reflectance from Landsat-8 Panchromatic images were corrected for solar zenith angle and mosaiced for validation. Panchromatic pixels are classified into three surface categories, i.e., open water & thin ice, refrozen leads, and pack ice, using Jenks natural breaks classification method (Jenks, 1963). In terms of turbulent heat flux, only pixels in the open water & thin ice category is regarded as leads. As can be seen in Table A1, the producer's accuracy of lead detection using iterative threshold is 89.5%, with an omission error of 10.5% and a commission error of 16.1%.

Appendix B

Constants

Constants used in IST calculation from Landsat-8 TIRS (Du et al. 2015)

1. MODIS emissivity library:
   $\varepsilon_{water,10}$=0.991; $\varepsilon_{water,11}$=0.986; $\varepsilon_{snow,10}$=0.986; $\varepsilon_{snow,11}$=0.959
   $\bar{\varepsilon}_{water}$=0.9885; $\Delta\varepsilon_{water}$ =0.005
   $\bar{\varepsilon}_{\mathrm{snow}}$=0.9725; $\Delta\varepsilon_{\mathrm{snow}}$ =0.027
2. NIR reflectance threshold for classification between water and ice/snow: 0.1
3. Water vapor content from MOD05: <2.5g/cm^2
4. *bi*: $b_{0\sim7}$: [-2.78009, 1.01408, 0.15833, -3.4991, 4.04487, 3.55414, -8.88394, 0.09152]
5. RMSE:0.34K

Constants used in turbulent heat flux estimation:

air density: $\rho_a = 1.3$ kg·m^{-3}
specific heat at constant pressure: $c_p = 1004$ J·kg^{-1}·K^{-1}
sensible heat transfer coefficient: $C_s = 0.00144$
evaporation coefficient: $C_e = 0.00144$
latent heat of vaporization: $L = 2.51 \times 10^6$ J·kg^{-1}
Reference height: $r = 2$m
gravitational constant: g=9.8m·s^{-2}
Salinity of sea water in the Beaufort Sea: S_w=27.947 (‰)
Freezing point of sea water:
$T_0 = 273.15 - 0.0137 - 0.05199S_w - 0.00007225S_w^2 = 271.68$
Wind speed profile fitting equation:

$$v_1 = v_2 \left(\frac{z_1}{z_2}\right)^a$$

where a=0.143, v_i and z_i(i=1, 2) represents wind speed and the altitude of measurements.

Author contribution. Xiaoping Pang and Xi Zhao designed the experiments and Meng Qu carried them out. Jinlun Zhang provide valuable instructions in data acquisition and manuscript editing. Qing Ji and Pei Fan helped develop the model code. Meng Qu prepared the manuscript with contributions from all co-authors.

Acknowledgements. This work was supported by the National Natural Science Foundation of China (Nos. 41876223, 41576188 and 41606215), and the National Key Research and Development Program of China (2016YFC1402704). The authors acknowledge the NASA Goddard Space Flight Center, the U.S. Geological Survey (USGS) and the European Center for Medium-Range Weather Forecasts (ECMWF) for providing the images and datasets used in this study.

Reference

Alam, A., and Curry, J. A.: Determination of surface turbulent fluxes over leads in Arctic sea ice. Journal of Geophysical Research: Oceans, 102(C2), 3331-3343, 1997.

Alam, A., and Curry, J. A.: Evolution of new ice and turbulent fluxes over freezing winter leads. Journal of Geophysical Research: Oceans, 103(C8), 15783-15802, 1998.

Andreas, E. L., and Cash, B. A.: Convective heat transfer over wintertime leads and polynyas. Journal of Geophysical Research: Oceans, 104(C11), 25721-25734, 1999.

Andreas, E. L., and Murphy, B.: Bulk transfer coefficients for heat and momentum over leads and polynyas. Journal of physical oceanography, 16(11), 1875-1883, 1986.

Andreas, E. L., Paulson, C. A., William, R. M., Lindsay, R. W., and Businger, J. A.: The turbulent heat flux from Arctic leads. Boundary-Layer Meteorology, 17(1), 57-91, 1979.

Arvidson, T., Gasch, J., and Goward, S. N.: Landsat 7's long-term acquisition plan — An innovative approach to building a global imagery archive. Remote Sensing of Environment, 78, 13–26, 2001.

Barsi, J. A., Schott, J. R., Hook, S. J., Raqueno, N. G., Markham, B. L., and Radocinski, R. G.: Landsat-8 thermal infrared sensor (TIRS) vicarious radiometric calibration. Remote Sensing, 6(11), 11607-11626, 2014.

Canadian Ice Service.: MANICE: Manual of standard procedures for observing and reporting ice conditions. Ice Services Branch, Atmospheric Environment Service, Ice Centre Environment Canada, Ottawa, Ontario, Canada, 2005.

Du, C., Ren, H., Qin, Q., Meng, J., and Zhao, S.: A practical split-window algorithm for estimating land surface temperature from Landsat 8 data. Remote Sensing, 7(1), 647-665, 2015.

Eppler, D. T., and Full, W. E.: Polynomial trend surface analysis applied to AVHRR images to improve definition of arctic leads. Remote Sensing of Environment, 40, 197-218, 1992.

Fett, R. W., Englebretson, R. E., and Burk, S. D.: Techniques for analyzing lead condition in visible, infrared and microwave satellite imagery. Journal of Geophysical Research: Atmospheres, 102(D12), 13657-13671, 1997.

Fetterer, F. M., and Holyer, R. J.: A Hough Transform Technique for Extracting Lead Features from Sea Ice Imagery. In Geoscience and Remote Sensing Symposium, 1989. IGARSS'89. 12th Canadian Symposium on Remote Sensing., 1989 International (Vol. 2, pp. 1125-1128). IEEE, 1989.

Fily, M., and Rothrock, D. A.: Opening and closing of sea ice leads: Digital measurements from synthetic aperture radar. Journal of Geophysical Research: Oceans, 95(C1), 789-796, 1990.

Gerace, A., and Montanaro, M.: Derivation and validation of the stray light correction algorithm for the thermal infrared sensor onboard Landsat 8. Remote sensing of environment, 191, 246-257, 2017.

Hall, D. K., Riggs, G. A., Salomonson, V. V., Barton, J. S., Casey, K., Chien, J. Y. L., ... and Tait, A. B.: Algorithm theoretical basis document (ATBD) for the MODIS snow and sea ice-mapping algorithms. Nasa Gsfc, 45, 2001.

Jenks, G. F.: Generalization in statistical mapping. Annals of the Association of American Geographers, 53 (1): 15–26, 1963.

Key, J., and Peckham, S.: Probable errors in width distributions of sea ice leads measured along a transect, Journal of Geophysical Research: Oceans, 96(C10), 18417-18423, 1991.

Key, J. R., Collins, J. B., Fowler, C., and Stone, R. S.: High-latitude surface temperature estimates from thermal satellite data. Remote Sensing of Environment, 61(2), 302-309, 1997.

Key, J., Maslanik, J. A., and Ellefsen, E.: The effects of sensor field-of-view on the geometrical characteristics of sea ice leads and implications for large-area heat flux estimates. Remote sensing of environment, 48(3), 347-357, 1994.

Key, J., Stone, R., Maslanik, J., and Ellefsen, E.: The detectability of sea-ice leads in satellite data as a function of atmospheric conditions and measurement scale. Annals of Glaciology, 17, 227-232, 1993.

Kwok, R.: Deformation of the Arctic ocean sea ice cover between November 1996 and April 1997: a qualitative survey. IUTAM symposium on scaling laws in ice mechanics and ice dynamics. Springer, Dordrecht. 315-322, 2001.

Kwok, R., and Rothrock, D. A.: Decline in Arctic sea ice thickness from submarine and ICESat records: 1958–2008. Geophysical Research Letters, 36(15), L15501, doi: 10.1029/2009GL039035, 2009.

Lindsay, R. W., & Rothrock, D. A.: Arctic sea ice surface temperature from AVHRR. Journal of Climate, 7(1), 174-183, 1994.

Lindsay, R. W., and Rothrock, D. A.: Arctic sea ice leads from advanced very high resolution radiometer images. Journal of Geophysical Research: Oceans, 100(C3), 4533-4544, 1995.

Marcq, S., and Weiss, J.: Influence of sea ice lead-width distribution on turbulent heat transfer between the ocean and the atmosphere. The Cryosphere, 6, 143-156, 2012.

Marsan, D., Stern, H., Lindsay, R., and Weiss, J.: Scale dependence and localization of the deformation of Arctic sea ice. Physical review letters, 93(17), 178501, 2004.

Maslanik, J. A., and Key, J.: On treatments of fetch and stability sensitivity in large-area estimates of sensible heat flux over sea ice. Journal of Geophysical Research: Oceans, 100(C3), 4573-4584, 1995.

Maykut, G. A.: Energy exchange over young sea ice in the central Arctic. Journal of Geophysical Research: Oceans, 83(C7), 3646-3658, 1978.

Maykut, G. A. The surface heat and mass balance. The geophysics of sea ice. Springer, Boston, MA. 395-463, 1986.

Miles, M. W., and Barry, R. G.: A 5-year satellite climatology of winter sea ice leads in the western Arctic. Journal of Geophysical Research: Oceans, 103(C10), 21723-21734, 1998.

Montanaro, M., Gerace, A., Lunsford, A., and Reuter, D.: Stray light artifacts in imagery from the Landsat 8 Thermal Infrared Sensor. Remote Sensing, 6(11), 10435-10456, 2014a.

Montanaro, M., Gerace, A., and Rohrbach, S.: Toward an operational stray light correction for the Landsat 8 Thermal Infrared Sensor. Applied Optics, 54(13), 3963-3978, 2015.

Montanaro, M., Levy, R., and Markham, B.: On-orbit radiometric performance of the Landsat 8 Thermal Infrared Sensor. Remote Sensing, 6(12), 11753-11769, 2014b.

Montanaro, M., Lunsford, A., Tesfaye, Z., Wenny, B., and Reuter, D.: Radiometric calibration methodology of the Landsat 8 thermal infrared sensor. Remote Sensing, 6(9), 8803-8821, 2014c.

Murashkin, D., Spreen, G., Huntemann, M., and Dierking, W.: Method for detection of leads from Sentinel-1 SAR images. Annals of Glaciology, 1-13, 2018.

Rampal, P., Weiss, J., and Marsan, D.: Positive trend in the mean speed and deformation rate of Arctic sea ice, 1979–2007. Journal of Geophysical Research: Oceans, 114(C5), C05013, doi: 10.1029/2008JC005066, 2009.

Ridler, T. W., and Calvard, S.: Picture thresholding using an iterative selection method. IEEE trans syst Man Cybern, 8(8), 630-632, 1978.

Röhrs, J., and Kaleschke, L.: An algorithm to detect sea ice leads by using AMSR-E passive microwave imagery. The Cryosphere, 6(2), 343-352, 2012.

Spreen, G., Kwok, R., and Menemenlis, D.: Trends in Arctic sea ice drift and role of wind forcing: 1992–2009. Geophysical Research Letters, 38(19), 2011.

Stull, R. B.: An introduction to boundary layer meteorology (Vol. 13). Springer Science and Business Media. 2012.

Tschudi, M. A., Curry, J. A., and Maslanik, J. A.: Characterization of springtime leads in the Beaufort/Chukchi Seas from airborne and satellite observations during FIRE/SHEBA. Journal of Geophysical Research: Oceans, 107(C10), 8034, doi: 10.1029/2000JC000541, 2002.

Venkatram, A.: A model of internal boundary-layer development. Boundary-Layer Meteorology, 11(4), 419-437, 1977.

Wadhams, P.: Sea-ice topography of the Arctic Ocean in the region 70 W to 25 E, Philos. Trans. R. Soc. London A, 302, 45-85, 1981.

Wadhams, P., McLaren, A. S., and Weintraub, R.: Ice thickness distribution in Davis Strait in February from submarine sonar profiles, Journal of Geophysical Research: Ocean, 90, 1069-1077, 1985.

Walter, B. A., Overland, J. E., and Turet, P.: A comparison of satellite ‐ derived and aircraft ‐ measured regional surface sensible heat fluxes over the Beaufort Sea. Journal of Geophysical Research: Oceans, 100(C3), 4585-4591, 1995.

Willmes, S., and Heinemann, G.: Pan-Arctic lead detection from MODIS thermal infrared imagery. Annals of Glaciology, 56(69), 29-37, 2015.

Weiss, J., and Marsan, D.: Scale properties of sea ice deformation and fracturing. Comptes Rendus Physique, 5(7), 735-751, 2004.

Wernecke, A., and Kaleschke, L.: Lead detection in Arctic sea ice from CryoSat-2: quality assessment, lead area fraction and width distribution. The Cryosphere, 9(5), 1955-1968, 2015.

World Meteorological Organization.: WMO - No. 259: Sea-Ice Nomenclature, volumes I, II and III. Oostende, Belgium. 2014.

Figure Captions

Figure 1. Location of study area. The background image is brightness temperature from MODIS Band31(~11 μm). Location of Landsat-8 images are marked by a red rectangle.

Figure 2. Detection of lead width using two orthogonal directions. Lead extent in orthogonal system (*v* and *h* direction) are

measured as x_1 and x_2, respectively.

Figure 3. Turbulent heat flux rises with increasing temperature difference $\triangle t$ and intense wind at lead width of 30m. Solid lines and dash lines represent sensible heat and latent heat respectively. Wind speed is illustrated by the color of the lines. Clearly, Sensible heat flux is basically proportional to $\triangle t$.

Figure 4. Turbulent heat flux for each width at wind speed of 5m/s. Temperature difference between the air and lead surface is marked by the color of the lines.

Figure 5. IST maps from MODIS and TIRS using split-window algorithms. (a) IST map from MODIS. (b) IST map from Landsat-8 TIRS. (c) Corrected IST map from TIRS.

Figure 6. Local median and noise image from TIRS IST. (a) Along track median temperature map. (b) noise image by detrend of the median temperature map.

Figure 7. Correlation between IST from MODIS and Landsat-8 TIRS before and after correction for straylight. The black lines are reference for x = y, and the red lines are linear regression lines with a fitting equation. The number density of scattered points is marked by color. (a) Scatter plot of IST from MODIS and Landsat-8 TIRS using split-window algorithm. (b) Scatter plot of IST from MODIS and corrected IST from Landsat-8 TIRS.

Figure 8. Temperature anomaly from MODIS and TIRS. (a) Local temperature anomaly from MODIS. (b) Local temperature anomaly from Landsat-8 TIRS.

Figure 9. Binary lead maps from MODIS and TIRS. (a) Binary lead map from MODIS. (b) Binary lead map from Landsat-8 TIRS.

Figure 10. Width distribution of leads from MODIS and TIRS in log-log plot. Data points from MODIS and TIRS are plotted as orange and blue dots, respectively. Power law fitting is applied. Fitting equations and R squares are shown for comparison.

Figure 11. Heat flux from MODIS and Landsat-8 using bulk formulae and fetch-limited model. (a) Turbulent heat flux from MODIS using bulk formulae. (b) Turbulent heat flux from Landsat-8 TIRS using bulk formulae. (c) Turbulent heat flux from Landsat-8 TIRS using fetch-limited model.

Figure 12. Distribution of 2 m air temperature over leads and surface temperature of all leads, small leads with width <1km, and larger leads with width <5km.

Figure 13. Contribution of heat flux from each lead width using bulk formulae and fetch-limited model. Turbulent heat flux retrieved using fetch-limited model and bulk formulae are plotted using solid lines and dash lines, respectively. Heat fluxes calculated using satellite surface temperature, air temperature and wind speed from reanalysis datasets are drawn in orange, simulated heat flux at $\triangle t$ = 5K and 10K are rendered in blue and green, respectively.

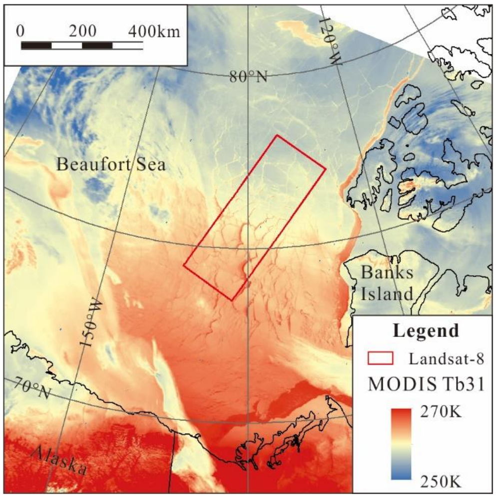

Figure 1. Location of study area. The background image is brightness temperature from MODIS Band31(~11 μm). Location of Landsat-8 images are marked by a red rectangle.

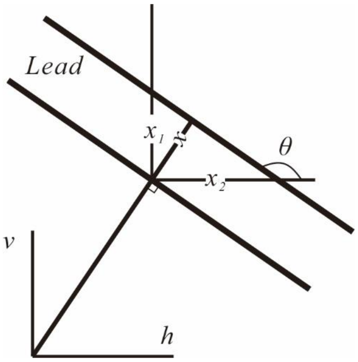

Figure 2. Detection of lead width using two orthogonal directions. Lead extent in orthogonal system (*v* and *h* direction) are measured as x_1 and x_2, respectively.

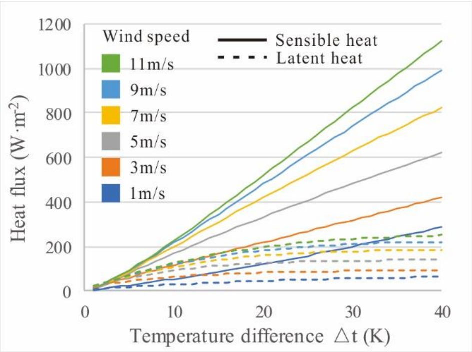

Figure 3. Turbulent heat flux rises with increasing temperature difference △t and stronger wind at lead width of 30m. Solid lines and dash lines represent sensible heat and latent heat respectively. Wind speed is illustrated by the color of the lines. Clearly, Sensible heat flux is basically proportional to △t.

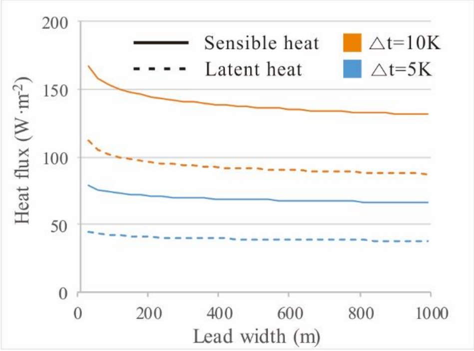

Figure 4. Turbulent heat flux for each width at wind speed of 5m/s. Temperature difference between the air and lead surface is marked by the color of the lines.

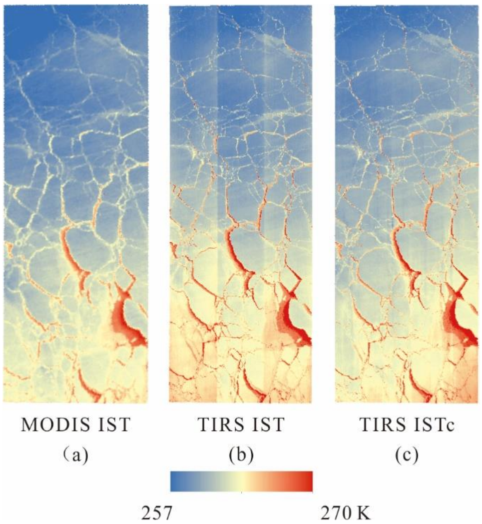

Figure 5. IST maps from MODIS and TIRS using split-window algorithms. (a) IST map from MODIS. (b) IST map from Landsat-8 TIRS. (c) Corrected IST map from TIRS.

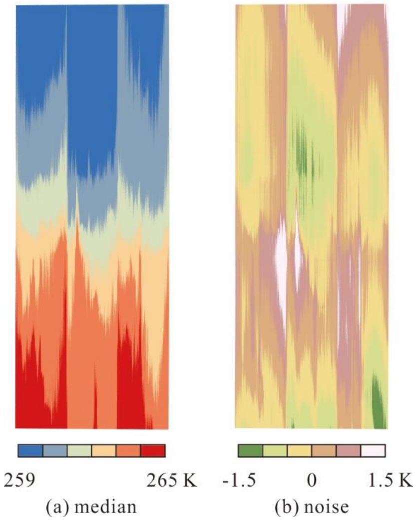

5 **Figure 6. Local median and noise image from TIRS IST. (a) Along track median temperature map. (b) noise image by detrend of the median temperature map.**

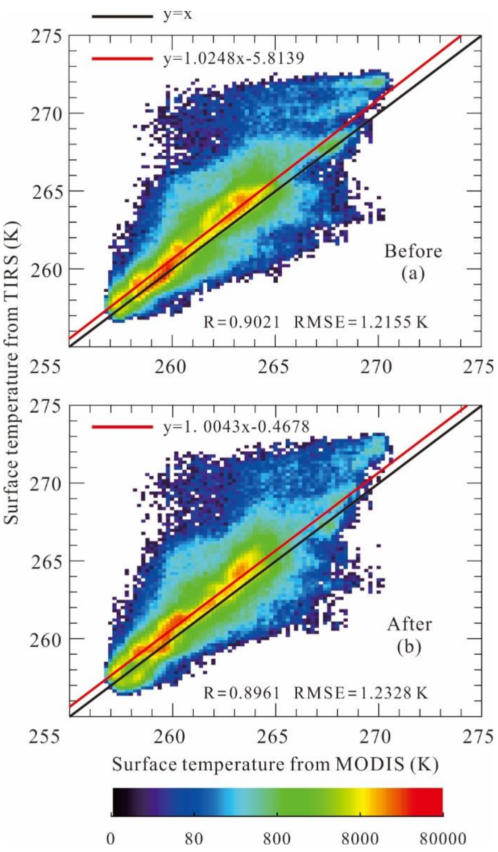

Figure 7. Correlation between IST from MODIS and Landsat-8 TIRS before and after correction for straylight. The black lines are reference for x = y, and the red lines are linear regression lines with a fitting equation. The number density of scattered points are marked by color. (a) Scatter plot of IST from MODIS and Landsat-8 TIRS using split-window algorithm. (b) Scatter plot of
5 **IST from MODIS and corrected IST from Landsat-8 TIRS.**

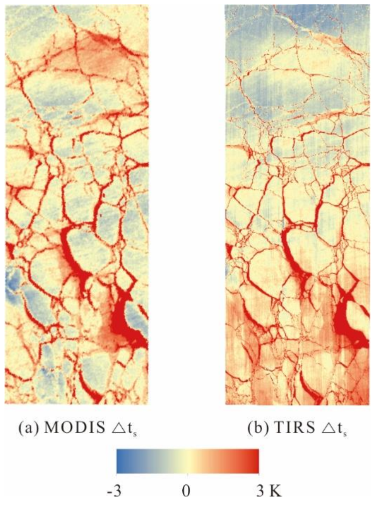

Figure 8. Temperature anomaly from MODIS and TIRS. (a) Local temperature anomaly from MODIS. (b) Local temperature anomaly from Landsat-8 TIRS.

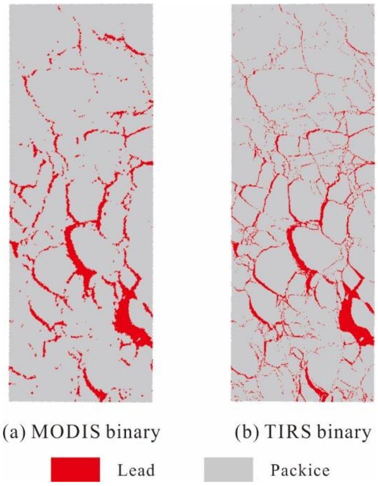

(a) MODIS binary (b) TIRS binary

Figure 9. Binary lead maps from MODIS and TIRS. (a) Binary lead map from MODIS. (b) Binary lead map from Landsat-8 TIRS.

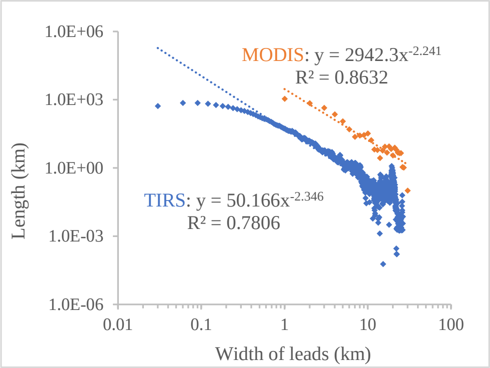

Figure 10. Width distribution of leads from MODIS and TIRS in log-log plot. Data points from MODIS and TIRS are plotted as orange and blue dots, respectively. Power law fitting is applied. Fitting equations and R squares are shown for comparison.

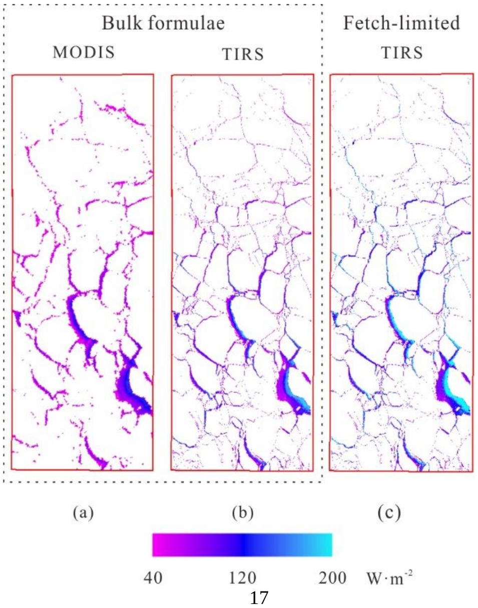

Figure 11. Heat flux from MODIS and Landsat-8 using bulk formulae and fetch-limited model. (a) Turbulent heat flux from MODIS using bulk formulae. (b) Turbulent heat flux from Landsat-8 TIRS using bulk formulae. (c) Turbulent heat flux from Landsat-8 TIRS using fetch-limited model.

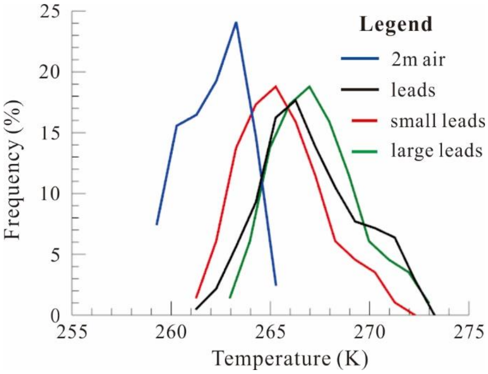

Figure 12. Distribution of 2 m air temperature over leads and surface temperature of all leads, narrow leads with width <1km, and larger leads with width >5km.

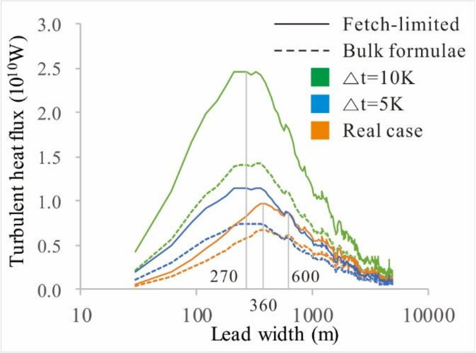

Figure 13. Contribution of heat flux from each lead width using bulk formulae and fetch-limited model. Turbulent heat flux retrieved using fetch-limited model and bulk formulae are plotted using solid lines and dash lines, respectively. Heat fluxes calculated using satellite surface temperature, air temperature and wind speed from reanalysis datasets are drawn in orange, simulated heat flux at ∆t = 5K and 10K are rendered in blue and green, respectively.

Table

Table 1. Satellite images and other data used in this study.

Resource	Parameters	Spatial-resolution	Time	Notes
Landsat-8 TIRS	Band5	30m	21:27	near-infrared
	Band8	15m	21:27	Panchromatic
	Band10	30m	21:27	10.60μm-11.19μm
	Band11	30m	21:27	11.50μm-12.51μm
Terra MODIS	Band31	1000m	20:55	10.78μm–11.28μm
	Band32	1000m	20:55	11.77μm–12.27μm
ERA-interim Reanalysis	10m wind	0.125°(~10km)	21:00	
	2m air temperature	0.125°(~10km)	21:00	
	2m dewpoint temperature	0.125°(~10km)	21:00	

Table 2. Turbulent heat flux from MODIS and TIRS using bulk formulae.

Sensors	range	Length (km)	Area		Heat flux	
			(km^2)	Contribution	(W)	Contribution

MODIS	all	2817	8074		4.63E+11	
	≤1km	1050.0	1050.0	13.00%	3.28E+10	7.08%
	1km~5km	1438.1	4065.0	50.35%	1.91E+11	41.16%
	>5km	258.3	2959.0	36.65%	2.40E+11	51.76%
TIRS	all	10150.3	7376.2		6.59E+11	
	≤1km	8502.2	2547.7	34.54%	1.68E+11	25.54%
	1km~5km	1440.7	2825.3	38.30%	2.62E+11	39.79%
	>5km	207.4	2003.3	27.16%	2.28E+11	34.67%

Table 3. Total heat flux from Landsat-8 using width -dependent and -independent model.

Lead category according to width	Areal fraction	Fetch-limited		Bulk formulae	
		Flux(W)	contribution	Flux(W)	contribution
Small: <1km	34.54%	2.39E+11	27.46%	1.68E+11	25.54%
Medium: 1km~5km	38.30%	3.47E+11	39.92%	2.62E+11	39.79%
Large: >5km	27.16%	2.83E+11	32.62%	2.28E+11	34.67%
total		8.69E+11		6.59E+11	

Table 4. Heat flux (W) contribution from different lead category.

	Lead category	Real case		△T=5K, u=5m/s		△T=10K, u=5m/s	
		Heat flux	Contribution	Heat flux	Contribution	Heat flux	Contribution
Bulk formulae	<1km	1.68E+11	25.54%	1.83E+11	34.54%	3.47E+11	34.54%
	1~5km	2.62E+11	39.79%	2.02E+11	38.30%	3.84E+11	38.30%
	<5km	2.28E+11	34.67%	1.44E+11	27.16%	2.72E+11	27.16%
	total	6.59E+11		5.29E+11		1.00E+12	
Fetch-limited	<1km	2.39E+11	27.46%	2.78E+11	36.54%	5.91E+11	37.18%
	1~5km	3.47E+11	39.92%	2.86E+11	37.64%	5.94E+11	37.40%
	<5km	2.83E+11	32.62%	1.96E+11	25.81%	4.04E+11	25.42%
	total	8.69E+11		7.60E+11		1.59E+12	

Table 5. Threshold candidates for lead detection and corresponding lead fraction.

		Fixed1	Fixed2	Fixed3	1st Std	2nd Std	3rd Std	iterative
MODIS	Threshold (K)	1	2	3	1.29	2.47	3.65	1.52
	Lead fraction	12.59%	6.04%	3.69%	9.73%	4.73%	2.71%	8.25%
TIRS	Threshold (K)	1	2	3	1.90	3.52	5.14	2.49
	Lead fraction	14.85%	8.65%	6.62%	8.93%	5.69%	2.82%	7.53%

Table A1. Leads and pack ice pixels detected by Landsat-8 TIRS and Panchromatic images at 15m resolution.

TIRS Panchromatic	Leads	Pack ice	total	Producer's Accuracy
Open water & thin ice	27039061	3172911	30211972	89.5%
Refrozen lead	4710542	41620953	46331495	
Pack ice	471960	368561891	369033851	
total	32221563	413355756	445577319	
User's Accuracy	83.9%			